ROYAL SOCIETY OF CHEMISTRY

Check for updates

Structural insight into an atomic layer deposition (ALD) grown Al_2O_3 layer on Ni/SiO_2: impact on catalytic activity and stability in dry reforming of methane†

Sung Min Kim, [ID] ‡[a] Andac Armutlulu, [ID][a] Wei-Chih Liao,§[b] Davood Hosseini,[a] Dragos Stoian, [ID][c] Zixuan Chen,[a] Paula M. Abdala, [ID][a] Christophe Copéret [ID][b] and Christoph Müller [ID]*[a]

The development of stable Ni-based dry reforming of methane (DRM) catalysts is a key challenge owing to the high operating temperatures of the process and the propensity of Ni for promoting carbon deposition. In this work, Al_2O_3-coated Ni/SiO_2 catalysts have been developed by employing atomic layer deposition (ALD). The structure of the catalyst at each individual preparation step was characterized in detail through a combination of *in situ* XAS–XRD, *ex situ* ^{27}Al NMR and Raman spectroscopy. Specifically, in the calcination step, the ALD-grown Al_2O_3 layer reacts with the SiO_2 support and Ni, forming aluminosilicate and $NiAl_2O_4$. The Al_2O_3-coated Ni/SiO_2 catalyst exhibits an improved stability for DRM when compared to the benchmark Ni/SiO_2 and Ni/Al_2O_3 catalysts. *In situ* XAS–XRD during DRM together with *ex situ* Raman spectroscopy and TEM of the spent catalysts confirm that the ALD-grown Al_2O_3 layer suppresses the sintering of Ni, in turn reducing also coke formation significantly. In addition, the formation of an amorphous aluminosilicate phase by the reaction of the ALD-grown Al_2O_3 layer with the SiO_2 support inhibited catalysts deactivation *via* $NiAl_2O_4$ formation, in contrast to the reference Ni/Al_2O_3 system. The in-depth structural characterization of the catalysts provided an insight into the structural dynamics of the ALD-grown Al_2O_3 layer, which reacts both with the support and the active metal, allowing to rationalize the high stability of the catalyst under the harsh DRM conditions.

1. Introduction

To mitigate anthropogenic climate change, carbon dioxide capture, storage and utilization (CCSU) is a promising technology.[1–5] In this context the dry reforming of methane (DRM) has emerged as a process to convert two major greenhouse gases, CH_4 and CO_2, into a synthesis gas (CH_4 + CO_2 → 2CO + 2H₂ ΔH^0_{298K} = +247 kJ mol^{-1}). Synthesis gas is a versatile chemical feedstock that can be converted further into synthetic liquid fuels and chemicals, *e.g.*, *via* the Fischer–Tropsch process.[6,7] In DRM the development of Ni-

based catalyst has received considerable attention, owing to its high activity combined with its relatively low cost when compared to noble metals.[8]

Ni^0 is proposed to be the catalytically active state for DRM, and a linear relationship between the DRM activity and the quantity of surface Ni has been reported.[5,9–12] However, under DRM conditions, Ni-based catalysts are prone to rapid deactivation due to a combination of various factors including coke formation,[13,14] metal oxidation followed by the migration of Ni into the support,[11,15–17] and sintering of the Ni particles.[18,19] The fact that the Tammann temperature of Ni (≈700 °C) is below the envisioned operating temperatures of the DRM process (≈900 °C) makes sintering a serious issue. Coke formation during DRM can proceed through methane decomposition (CH_4 → C + 2H₂, ΔH^0_{298K} = +75 kJ mol^{-1}) and CO disproportionation, *i.e.*, Boudouard reaction (2CO → C + CO_2, ΔH^0_{298K} = −171 kJ mol^{-1}). Carbon species accumulate on the catalyst surface thereby blocking the active sites for DRM or leading to the detachment of Ni particles from the support. Coke formation is also linked to sintering since the nature and the rate of coke deposition is

[a] Department of Mechanical and Process Engineering, ETH Zurich, Leonhardstrasse 27, 8092 Zurich, Switzerland. E-mail: muelchri@ethz.ch
[b] Department of Chemistry and Applied Sciences, ETH Zurich, Vladimir Prelog Weg 1-5, 8093 Zurich, Switzerland
[c] Swiss–Norwegian Beamlines, ESRF, BP 220, Grenoble, 38043, France
† Electronic supplementary information (ESI) available. See DOI: 10.1039/d1cy01149a
‡ Institute for Integrated Catalysis, Pacific Northwest National Laboratory, Richland, Washington 99352, USA.
§ DSM Applied Science Center, P.O. Box 1066, 6160 BB Geleen, The Netherlands.

This journal is © The Royal Society of Chemistry 2021

Catal. Sci. Technol., 2021, **11**, 7563–7577 | 7563

sensitive to the size of the Ni nanoparticles.[20,21] When Ni (111) facets and step edges are too small, nucleation of C* does not proceed, restricting the formation of a graphene layer.[20] Thus, the formation and the stabilization of small Ni particles (<10 nm) is a key requirement towards the development of highly active and stable Ni-based DRM catalysts.[21–24] A further challenge with regards to Ni-based DRM catalysts that has to be overcome is the inhibition of the reaction of Ni with the (metal oxide) support. Although Al_2O_3 support is known to stabilize Ni particles more effectively against sintering than SiO_2, the reaction of Ni with Al_2O_3 can lead to its oxidation and formation of inactive $NiAl_2O_4$.[11,15,16] Hence conceiving and generating highly active and stable Ni-based DRM catalysts, several strategies have been proposed, including (i) controlling the Ni particle size with the aim of minimizing the fraction of edge and step sites on the nickel surface;[11,22,25] (ii) coating Ni-based DRM catalyst by metal oxide layers (*e.g.*, Al_2O_3, MgO, ZrO_2 and SiO_2)[13,26–32] to alleviate sintering and coke formation; (iii) deposition of Ni particles on basic supports (*e.g.*, MgO and La_2O_3) to reduce coke formation;[11,16] (iv) promotion with alkaline (*e.g.*, K and Na),[33,34] alkaline earth (*e.g.*, Mg, Ca and Ba)[33,35] or lanthanide (*e.g.* La)[16,36] metals to facilitate CO_2 activation to gasify carbon; and (v) the alloying of Ni with a noble (*e.g.*, Pt, Rh, Pd, and Ru)[37–41] or non-noble (*e.g.*, Fe, Cu, Mn, and Co)[9,10,37,42–44] transition metal to improve its activity and stability for DRM.

SiO_2-Supported Ni DRM catalysts have been plagued by a lower metal dispersion and poor sintering resistance under DRM conditions owing to a weak metal–support interaction.[45] To stabilize Ni nanoparticles on a SiO_2 support, several strategies have been employed. For example, nickel-silicide colloids have been deposited on SiO_2 and CeO_2 supports. Treatment in H_2 leads to the formation of small, supported Ni nanoparticles (1–2 nm).[25] Further, the addition of metal oxide overcoats (SiO_2, Al_2O_3, MgO, ZrO_2 and TiO_2)[13,26,27] on Ni/SiO_2 has shown to reduce sintering and coke formation.

In order to precisely control the thickness of the metal oxide overcoat with atomic scale precision, atomic layer deposition (ALD) has been employed.[46] ALD-grown TiO_2,[28] Al_2O_3[30,31] and ZrO_2[29] coatings demonstrated an enhanced catalytic activity and stability. Although the deposition of Al_2O_3 coating onto Ni/Al_2O_3[26] alleviated the sintering of Ni under DRM conditions, Ni was found to interact with the overcoat to form $NiAl_2O_4$. Currently, the structural and electronic interaction of Ni with an Al_2O_3 overcoat is only poorly understood, hindering the further development of this class of material systems.

This work aims at obtaining an atomic-level understanding of how an ALD-grown Al_2O_3 overcoat reacts with Ni and the SiO_2 support during pretreatment and DRM. To this end, Al_2O_3-coated Ni/SiO_2 DRM catalysts have been obtained by ALD. The structure of the catalysts were interrogated in detail by *in situ* X-ray absorption spectroscopy (XAS) and X-ray powder diffraction (XRD) to probe the local structure of Ni, the average crystalline structure and changes therein with time-on-stream (TOS) during catalyst pretreatment and DRM. Further spectroscopic (Raman, FTIR and [27]Al magic-angle spinning (MAS) solid-state NMR) and electron microscopy (TEM) characterizations were applied to scrutinize the structural dynamics of the Al_2O_3 coating during synthesis and pretreatment and to elucidate the driving forces behind sintering and coking under DRM conditions.

2. Experimental

2.1. Preparation of bare Ni/SiO₂ and Ni/Al₂O₃ catalysts

5 wt% Ni/SiO_2 and Ni/Al_2O_3 catalysts were prepared by incipient wetness impregnation using $Ni(NO_3)_2$ as the Ni precursor and, respectively, Aerosil 300 SiO_2 (S_{BET} = 275 m^2 g^{-1}) and γ-Al_2O_3 (S_{BET} = 220 m^2 g^{-1}) supports. The catalysts were calcined at 300 °C under static air to yield NiO.

2.2. Atomic layer deposition of Al₂O₃

An Al_2O_3 overcoat was deposited onto calcined catalyst at 300 °C (NiO/SiO_2 and NiO/Al_2O_3) and onto the supports (SiO_2 and Al_2O_3) *via* ALD (Picosun R-200, equipped with a powder coating system). Electronic grade trimethylaluminum (TMA) and deionized (DI) water (or ozone) were used as the Al_2O_3 precursor and oxidants, respectively. High-purity N_2 served as both the carrier and purge gas. In a typical ALD deposition cycle the following pulse and purge (N_2) times were used: 0.1 s TMA – 15 s N_2 purge – 0.1 s oxidant (H_2O or O_3) – 15 s N_2 purge. The deposition was carried out at 300 °C. High-resolution TEM allowed us to determine the deposition rate, *i.e.*, ≈1.0 Å per ALD cycle, which is in good agreement with the thickness of an Al_2O_3 layer, grown simultaneously on a Si wafer and measured by ellipsometry (SENTECH SE850). To prepare the Al_2O_3-coated catalysts, approximately 300 mg of the catalyst (pre-calcined at 300 °C) were loaded into the reactor *via* a powder cartridge and then heated to 300 °C under vacuum, followed by repeated ALD cycles. The as-synthesized catalyst was subsequently calcined at 800 °C in static air in a muffle furnace.

2.3. Characterization

Elemental analysis. The elemental composition of the calcined materials was determined by inductively coupled plasma optical emission spectroscopy (ICP-OES, Agilent 5100 VDV) and inductively coupled plasma atomic emission spectrometry (ICP-AES, Thermo Fisher Scientific iCap 6500, Dual View).

Nitrogen physisorption. Nitrogen physisorption was performed in a NOVA 4000e (Quantachrome) instrument at −196 °C. Prior to the experiment, the samples were degassed at 300 °C under vacuum (10^{-3} mbar) for 3 h. The specific surface area and pore size distribution were calculated using the Brunauer–Emmett–Teller (BET) and Barrett–Joyner–Halenda (BJH) models, respectively.

7564 | *Catal. Sci. Technol.*, 2021, **11**, 7563–7577

This journal is © The Royal Society of Chemistry 2021

Hydrogen temperature-programmed reduction (H$_2$-TPR). H$_2$-TPR was conducted in Autochem 2920 equipped with a thermal conductivity detector (TCD). In a typical experiment, 50 mg of a calcined catalyst were loaded into a U-shaped quartz reactor and heated up to 1000 °C under a flow (50 ml min^{-1}) of 5 vol% H$_2$ in Ar. The concentration of H$_2$ in the off-gas was measured using a TCD after having passed through a cold trap (−10 °C).

Ammonia temperature-programmed desorption (NH$_3$-TPD). NH$_3$-TPD was conducted in Autochem 2920 equipped with a TCD detector. In a typical experiment, 50 mg of a calcined catalyst was loaded into a U-shape quartz reactor and subsequently heated to 500 °C in He (50 ml min^{-1}) for 1 h, followed by cooling down to 150 °C. The catalyst was then exposed to a flow (50 ml min^{-1}) of 5 vol% NH$_3$ in He for 1 h followed by a He purge (50 ml min^{-1}) for 1 h. The TPD profile of NH$_3$ was continuously recorded using a TCD.

Pyridine infrared spectroscopy (Py-IR). The infrared (IR) spectra of the samples onto which pyridine was adsorbed were recorded with a Nicolet FTIR (Thermo Scientific) at a resolution of 4 cm^{-1}. The catalyst samples were prepared as self-supporting wafers and exposed to vacuum ($p = 10^{-6}$ mbar) at 450 °C for 1 h (heating rate of 10 °C min^{-1}). After cooling down to 150 °C, the sample was equilibrated with 0.1 mbar pyridine for 0.5 h followed by outgassing for 1 h and the acquisition of a spectrum. The concentrations of Brønsted (BAS) and Lewis acid sites (LAS) were quantified using the integrated areas under the peaks at 1540 cm^{-1} and 1450 cm^{-1}, respectively. For quantification, molar extinction coefficients of 0.73 cm μmol^{-1} and 0.96 cm μmol^{-1} were used for Brønsted and Lewis acid sites, respectively.[47]

Hydrogen chemisorption. H$_2$ chemisorption was conducted in Autochem 2920 equipped with a TCD detector. 50 mg of the calcined catalyst were loaded into a quartz reactor and reduced in 5 vol% H$_2$ in Ar at the temperature determined by H$_2$-TPR for 1 h. Subsequently, the sample was purged with Ar at 450 °C for 30 min in order to desorb H$_2$ on the surface followed by cooling down to 50 °C. The quantity of chemisorbed hydrogen was determined at 45 °C by periodically injecting pulses of 5 vol% H$_2$ in Ar over the reduced catalyst. The stoichiometry factor between dissociated H$_2$ and the active metal was assumed to be 1.0 (H/Ni).[48–50]

^{27}Al magic angle spinning solid-state nuclear magnetic resonance (^{27}Al MAS NMR). ^{27}Al solid state NMR spectra were obtained at a static field of 9.4 T (104.26 MHz of ^{27}Al operating frequency) with a Bruker 2.5 mm DR MAS probe. All ^{27}Al NMR chemical shifts were referenced externally to (NH$_4$)Al(SO$_4$)$_2$·12H$_2$O at −0.6 ppm. The sample spinning frequency was set to 25 kHz. ^{27}Al direct-excited spin-echo spectra were acquired with a recycle delay of 1 second. The excitation pulse was optimized to yield maximal signal intensity. One rotor period was used as the echo delay. The numbers of scans were adjusted to obtain good to moderate signal-to-noise ratios (ca. 8000 scans for 100 ALD cycles; ca. 40 000, 20 000, and 80 000 scans for calcined Al$_2$O$_3$-coated

SiO$_2$, Al$_2$O$_3$-coated NiO/SiO$_2$, and reduced Al$_2$O$_3$-coated Ni/SiO$_2$, respectively). The raw FID was shifted by 142 points towards the start of FID acquisition. All spectra were fitted with the CzSimple model using the DMFit software,[51] simulating the ^{27}Al central transitions with a Gaussian distribution of sites ($d = 5$).

X-ray absorption spectroscopy (XAS) and X-ray powder diffraction (XRD). In situ combined XAS (Ni K-edge, 8.2 keV)–XRD experiments were performed at the Swiss-Norwegian Beamlines (SNBL, BM31) at the European Synchrotron Radiation Facility (ESRF). The catalyst (≈2 mg) was loaded into a capillary quartz reactor (1.0 mm of outer diameter).[9] The as-synthesized catalyst was calcined in synthetic air (20 vol% O$_2$/N$_2$) at 800 °C. The calcined catalyst was then reduced at the temperature determined by H$_2$-TPR with a ramping rate of 10 °C min^{-1} under 10 vol% H$_2$/He (10 ml min^{-1}). Subsequently, the DRM reaction was performed at 700 °C in a total flow rate of 10 ml min^{-1} of the feed gas (4.5 ml min^{-1} CH$_4$, 4.5 ml min^{-1} CO$_2$ and 1 ml min^{-1} He). During reduction and DRM tests, XAS–XRD data were collected alternatingly. XAS spectra were collected at the Ni K-edge using a Si (111) double crystal monochromator in transmission mode. XRD data were collected with a 2D DEXELA detector using a Si (111) channel-cut monochromator set at a wavelength of 0.5060 Å. Alternating XAS–XRD data were collected during temperature-programmed calcination, reduction and DRM. For ex situ XAS measurements, the as-synthesized materials and references were mixed with cellulose (the sample to cellulose ratio was chosen such that XAS measurements in transmission mode were optimized) and ground to a fine powder. The pelletized samples were measured in transmission mode. The XAS data were analyzed using the Athena and Artemis software.

Electron microscopy. The morphology, particle size and particle composition of the reduced and reacted catalysts were analyzed by transmission electron microscopy (TEM, Philips CM 12, 100 kV), high-resolution transmission electron microscopy (HR-TEM, FEI F30 FEG, 300 kV) and scanning transmission electron microscopy (STEM, Hitachi HD-2700). TEM and STEM were operated at 200 kV, which were equipped with a SuperX EDX consisting of four SDD detectors.

Temperature-programmed oxidation (TPO). Temperature-programmed oxidation (TPO) and carbon deposition experiments were performed in a thermogravimetric analyzer (TGA, Mettler Toledo TGA/DSC). A small amount of the reacted catalyst (≈15 mg) was placed in an alumina crucible and heated to 1000 °C (10 °C min^{-1} ramp) under an air flow (50 ml min^{-1}). The weight loss of the reacted material during oxidation was recorded continuously.

Raman spectroscopy. Coke deposition was characterized by Raman spectroscopy (Thermo Scientific). The Raman spectra were acquired in the range 500–3500 cm^{-1} using a laser with a wavelength of 514.5 nm. The spectral resolution employed was 4 cm^{-1}.

This journal is © The Royal Society of Chemistry 2021

Catal. Sci. Technol., 2021, **11**, 7563–7577 | **7565**

2.4. DRM catalytic test

The DRM reaction was carried out in a fixed-bed quartz reactor (400 mm length, 12.6 mm internal diameter). The calcined catalyst ($\approx$20 mg) was loaded into the reactor and reduced at the temperature determined by H_2-TPR in 10 vol% H_2/N_2 (100 ml min^{-1}) for 2 h. Subsequently, the bed was cooled down to 700 °C to perform the DRM activity test. The total flow rate of the feed gas was 100 ml min^{-1} (270 L g^{-1} h^{-1}; 45 ml min^{-1} CH_4, 45 ml min^{-1} CO_2 and 10 ml min^{-1} N_2). The composition of the off-gas was analyzed by an online micro-GC equipped (CV-200, Thermo Scientific). N_2 was used as internal standard.

3. Results and discussion

3.1. Deposition of an Al_2O_3 overcoat onto Ni/SiO_2 by ALD

Fig. 1a schematically describes the surface reactions occurring during a half and full ALD cycle. To follow the surface reactions occurring during ALD, FTIR spectra were collected after one half (*i.e.*, after injection of a TMA pulse) and a full (*i.e.*, TMA and subsequent injection of a steam pulse) ALD cycle on dehydroxylated SiO_2 (Fig. 1b). Due to high reactivity of TMA with air and moisture, the FTIR measurements were carried out in an inert atmosphere (glovebox). SiO_2 dehydroxylated at 500 °C in high vacuum (10^{-6} mbar) shows isolated silanols at 3746 cm^{-1}. After one half cycle, *i.e.*, after pulsing TMA, the intensity of the peak from isolated silanols is significantly reduced owing to their reaction with TMA. In addition, peaks associated with C–H stretching vibrations (2916 and 2966 cm^{-1}) appear owing to methyl groups of surface-adsorbed (or chemisorbed) TMA. After injection of a pulse of steam, *i.e.*, after the completion of a full ALD cycle, the intensity of the peak due to isolated silanols restores, albeit with a reduced intensity. In addition, a new broad band between 3461–3498 cm^{-1} appears, which is ascribed to a O–H interacting with Al and Si on the surface (or vicinal silanols).[52] The regeneration of surface O–H groups provides the reactive sites for subsequent ALD cycles.
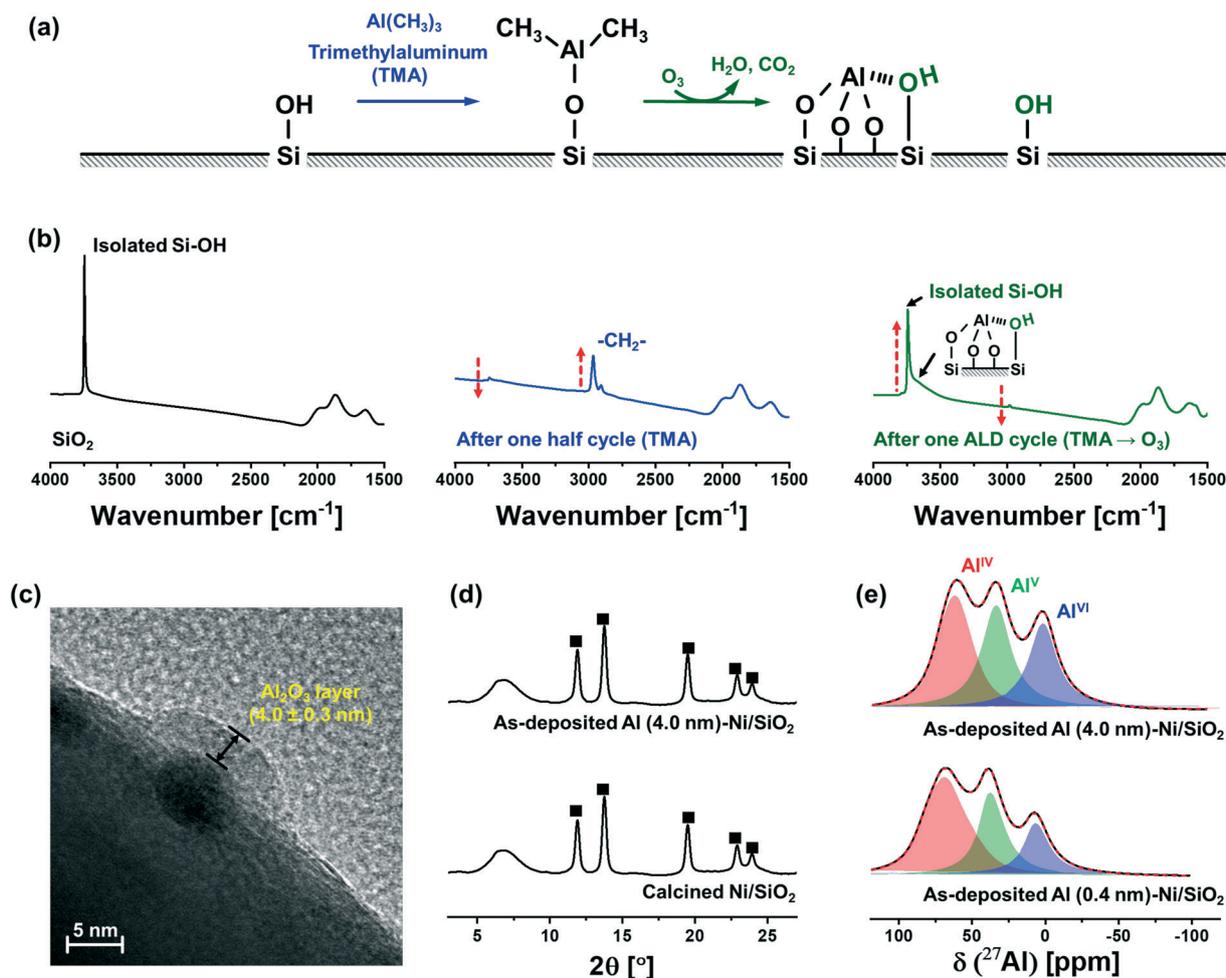
Fig. 1 Characterization of as-synthesized Al (0.4 nm)–Ni/SiO_2 and Al (4.0 nm)–Ni/SiO_2: (a) schematic illustrating the surface reactions occurring over a half and a full ALD cycle. (b) FTIR spectra obtained after a half and a full ALD cycle. The arrows indicate the direction of change during a full ALD cycle. (c) TEM image of Al (4.0 nm)–Ni/SiO_2, showing an amorphous Al_2O_3 layer on top of a Ni nanoparticle dispersed on a SiO_2 support. (d) XRD diffractograms of as-synthesized Al (4.0 nm)–Ni/SiO_2 and calcined Ni/SiO_2: (■) NiO. (e) Solid-state ^{27}Al NMR spectra of as-synthesized Al (0.4 nm)–Ni/SiO_2 and Al (4.0 nm)–Ni/SiO_2.

7566 | *Catal. Sci. Technol.*, 2021, **11**, 7563–7577

This journal is © The Royal Society of Chemistry 2021

The growth rate of the Al_2O_3 layer was estimated by HR-TEM (Fig. 1c). The thickness of the Al_2O_3 layer on Ni nanoparticle (5.0 ± 0.3 nm) supported on SiO_2 after 40 ALD cycles (TMA/steam) was determined as 4.0 ± 0.3 nm, denoted as Al (4.0 nm)–Ni/SiO_2, corresponding to a deposition rate of ~0.1 nm/ALD cycle.

XRD characterization of Ni/SiO_2 calcined at 300 °C and as-synthesized Al (4.0 nm)–Ni/SiO_2 (ALD temperature 300 °C) revealed the presence of cubic NiO ($Fm\bar{3}m$ space group) in Ni/SiO_2 (Fig. 1d). A broad halo at 4.5–9.5° is ascribed to the amorphous SiO_2 support. Similarly, in the case of as-synthesized Al (4.0 nm)–Ni/SiO_2, only Bragg peaks due to NiO are present, indicating an amorphous nature of the as-deposited Al_2O_3 layer.

As-synthesized, Al_2O_3-coated Ni/SiO_2 catalysts with different thicknesses of the Al_2O_3 layer (0.4 nm and 4.0 nm), i.e., Al (0.4 nm)–Ni/SiO_2 and Al (4.0 nm)–Ni/SiO_2, were characterized further by ^{27}Al MAS NMR (Fig. 1e). The fitting of the ^{27}Al MAS NMR spectra was performed using the Czjzek model.[51] The ^{27}Al MAS spectra of as-synthesized Al (0.4 nm)–Ni/SiO_2 and Al (4.0 nm)–Ni/SiO_2 contains tetra- (Al^{IV}, NMR shift δ = 75.9, 35.2, 8.6 ppm and quadrupolar coupling constant C_Q = 8.4 MHz, penta- (Al^V, δ = 35.2 ppm and C_Q = 6.3 MHz) and hexa- (Al^{VI}, δ = 8.6 ppm and C_Q = 5.7 MHz) coordinated Al sites, and no significant differences are observed between the spectra of as-synthesized Al (0.4 nm)–Ni/SiO_2 and Al (4.0 nm)–Ni/SiO_2. The broad and featureless ^{27}Al NMR line feature is characteristic of amorphous Al_2O_3,[53–55] in line with the absence of diffraction peaks due to Al_2O_3 in as-synthesized Al (4.0 nm)–Ni/SiO_2.

3.2. Structural characterization of the materials after calcination at 800 °C: probing the interaction of the Al_2O_3 layer with Ni and SiO_2

3.2.1. Physical, chemical, and textural properties of the calcined materials.
As-synthesized Ni/SiO_2, Al (0.4 nm)–Ni/SiO_2, and Al (4.0 nm)–Ni/SiO_2 were subsequently calcined at 800 °C in static air for 1 h. HAADF STEM with elemental mapping (Fig. S2†) confirms that in calcined Al (4.0 nm)–Ni/SiO_2 Al is distributed homogeneously on the surface of the silica, indicating that the ALD-grown Al_2O_3 layer maintains its highly dispersed character after calcination at 800 °C.

The elemental composition of the materials, as determined by ICP-OES, is summarized in Table 1. The deposition of an Al_2O_3 overcoat onto Ni/SiO_2 results in a reduction of the weight fractions of Ni (and SiO_2). Elemental analysis showed that the weight percent of Ni in the materials was reduced from 5 wt% in Ni/SiO_2 to 4.8 wt% and 3.7 wt% in Al (0.4 nm)–Ni/SiO_2 and Al (4.0 nm)–Ni/SiO_2, respectively (accompanied by an increase in the Al content from 0 wt%, to 1.1 wt% and 10.2 wt%).

The N_2 isotherms and BJH pore size distributions of Ni/SiO_2 calcined at 300 °C, as-synthesized Al (4.0 nm)–Ni/SiO_2, and Al (4.0 nm)–Ni/SiO_2 calcined at 800 °C are shown in Fig. S3.† The specific surface area and BJH pore volume of Ni/SiO_2 are 198 m^2 g^{-1} and 1.33 cm^3 g^{-1}, respectively. After the deposition of a 4 nm-thick layer of Al_2O_3 onto Ni/SiO_2, i.e., as-synthesized Al (4.0 nm)–Ni/SiO_2, the pore volume in pores with a diameter d_{pore} = 10–100 nm is significantly reduced (Fig. S3b†), resulting in a BET surface area and BJH pore volume of, respectively, 91 m^2 g^{-1} and 0.64 cm^3 g^{-1}. This reduction in surface area is ascribed to the filling of voids by the ALD-grown Al_2O_3. On the other hand, Al (4.0 nm)–Ni/SiO_2 after calcination (800 °C), shows a significant increase of the volume in small pores (d_{pore} = 1–10 nm) (Fig. S3b†). Such an increase in the specific surface area and BJH pore volume was also observed in calcined Al (0.4 nm)–Ni/SiO_2 (Table 1). We hypothesize that the local restructuring of the ALD-grown Al_2O_3 layer during calcination (including the reaction of the Al_2O_3 layer with NiO and SiO_2 as discussed in more detail in the following section) is responsible for the formation of additional small pores.

3.2.2. In situ XRD–XAS of Al (4.0 nm)–Ni/SiO_2 during calcination: $NiAl_2O_4$ formation.
To elucidate the chemical reaction between the ALD-grown Al_2O_3 layer and the Ni/SiO_2 catalyst, in situ synchrotron XRD–XAS measurements were performed during the calcination of as synthesized Al (4.0 nm)–Ni/SiO_2 (Fig. 2). Combined in situ XRD patterns and XANES spectra at the Ni K-edge were collected in an alternating fashion during the calcination ramp from room temperature to 800 °C with a rate of 10 °C min^{-1} in 20 vol% O_2/N_2, using a setup described elsewhere and schematized in Fig. S1.†[9,56] The in situ diffractogram of as synthesized Al (4.0 nm)–Ni/SiO_2 shows peaks due to a crystalline NiO phase, while no Bragg peaks due to crystalline Al_2O_3 were observed

Table 1 Physical and chemical properties of Ni/SiO_2 and the Al_2O_3-coated Ni/SiO_2 catalysts

Catalyst	Elemental composition[a]		N_2 physisorption[b]			Chemisorption		Ni particle size[d] [nm]	
	Ni [wt%]	Al [wt%]	S_{BET} [m^2 g^{-1}]	$V_{pore,BJH}$ [cm^3 g^{-1}]	D_{pore} [nm]	H_2 uptake[c] [μmol g^{-1}]	Dispersion [%]	H_2-Chem.	TEM
Ni/SiO_2	5.0	—	197	1.33	1.9	102	12	8.5	7.1 ± 1.8
Al (0.4 nm)–Ni/SiO_2	4.8	1.1	201	1.40	1.9	91	11	9.1	7.3 ± 1.5
Al (4.0 nm)–Ni/SiO_2	3.7	10.2	204	1.44	2.0	70	11	9.1	8.2 ± 1.1

[a] The weight percentage of Ni and Al in the calcined materials was determined by ICP-OES. [b] The specific surface area, pore volume, and pore radius were calculated using the BET and BJH models for the calcined materials. [c] The quantity of surface Ni in the reduced materials was determined by H_2 chemisorption using a stoichiometry factor of 1.0 for H/Ni. [d] The average Ni particle size of the reduced materials was determined by HR-TEM.
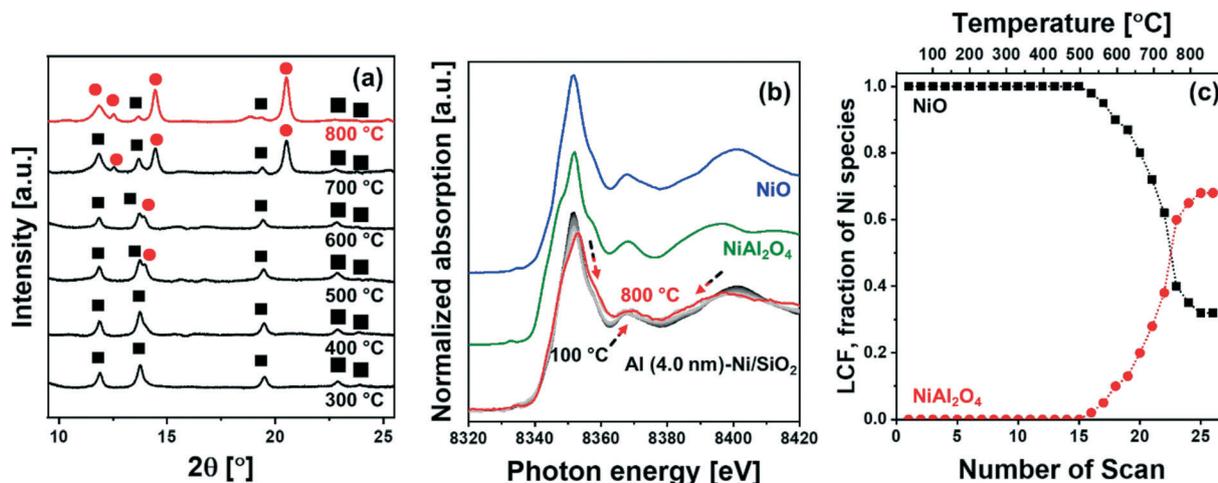
Fig. 2 Combined *in situ* XRD–XAS characterization: (a) *in situ* XRD (λ = 0.5060 Å), (b) *in situ* Ni K-edge XANES with NiO and $NiAl_2O_4$ references, and (c) corresponding LCF analysis results for Al (4.0 nm)–Ni/SiO_2 during calcination in 20 vol% O_2/N_2. The symbols in the diffractogram mark the peaks due to NiO (ICSD 9866, ■) and $NiAl_2O_4$ (ICSD 9554, ●). The arrows indicate the direction of change in the XANES spectra with increasing calcination temperature.

between 50–400 °C owing to the amorphous nature of the ALD-grown Al_2O_3 layer and the amorphous SiO_2 support. Bragg peaks due to spinel $NiAl_2O_4$ ($Fd\bar{3}m$ space group) started to appear at *ca.* 500 °C (Fig. 2a), which grew in intensity as the temperature increased to 800 °C; this was accompanied by a simultaneous decrease of the intensity of the NiO peaks. The diffraction pattern of $NiAl_2O_4$ is similar to that of γ-Al_2O_3, yet we can clearly assign the observed peaks to $NiAl_2O_4$ when taking into account the results of the analysis of the XANES spectra. For the *in situ* XANES spectra at the Ni K-edge during

calcination, the white line decreased in intensity and shifted from 8352 eV to 8354 eV (Fig. 2b). In addition, changes in the features of the post-edge region were observed, in line with the formation of $NiAl_2O_4$. NiO and $NiAl_2O_4$ exhibit very distinct XANES features as shown in Fig. 2b. Thus, applying linear combination fitting (LCF) analysis, using references for NiO and $NiAl_2O_4$ (Fig. 2b and c) revealed the onset of $NiAl_2O_4$ formation at *ca.* 500 °C. The fraction of $NiAl_2O_4$ reached 0.68 at 800 °C, whereas the fraction of NiO was reduced correspondingly. Hence *in situ* XRD–XAS experimentation
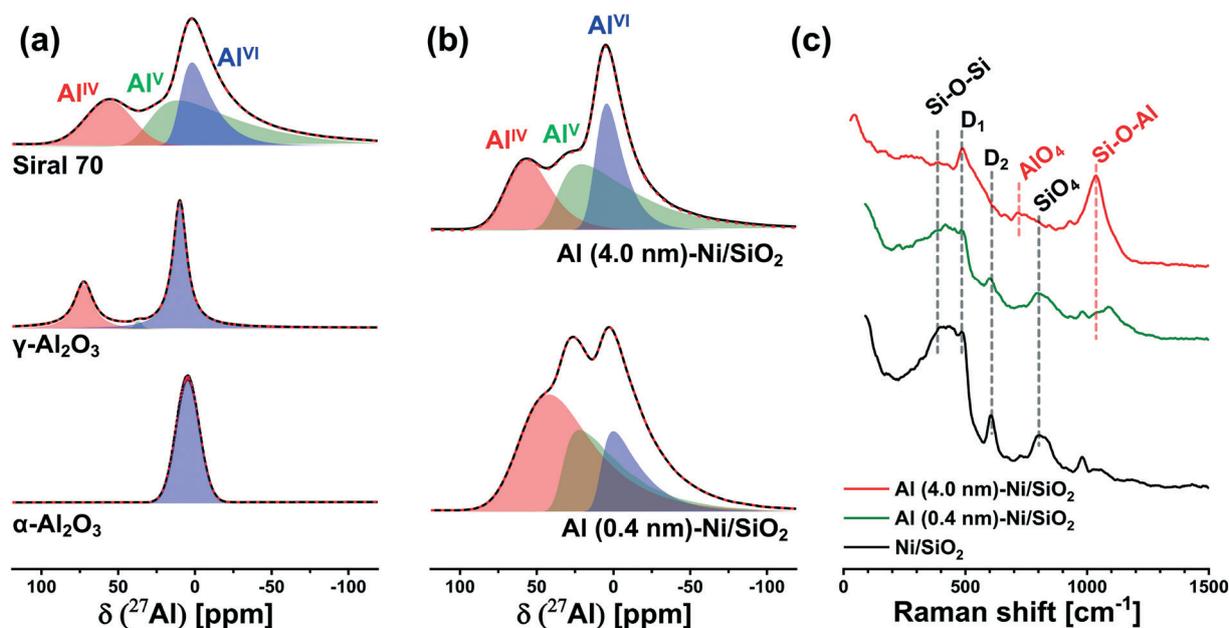
Fig. 3 Characterization of the interaction between silica and alumina: solid-state ^{27}Al-NMR of (a) α-Al_2O_3, γ-Al_2O_3, and aluminosilicate Siral 70 references; and (b) calcined Al (0.4 nm)–Ni/SiO_2 and Al (4.0 nm)–Ni/SiO_2. (c) Raman spectra of calcined Ni/SiO_2, Al (0.4 nm)–Ni/SiO_2, and Al (4.0 nm)–Ni/SiO_2.

7568 | *Catal. Sci. Technol.*, 2021, **11**, 7563–7577

This journal is © The Royal Society of Chemistry 2021

confirms the reaction of NiO with the ALD-grown Al_2O_3 layer forming $NiAl_2O_4$ (NiO + Al_2O_3 → $NiAl_2O_4$).[57] However it is worth noting that *in situ* XRD and Ni K-edge XANES only allows to elucidate the reaction between the ALD-grown Al_2O_3 and NiO and cannot probe the interaction between Al_2O_3 and the SiO_2 support. This is due to the fact that XAS is an element specific technique and Ni K-edge XAS can only probe the environment around Ni, while XRD is unable to provide any information on amorphous phases (such as amorphous aluminosilicates).

3.2.3. ssNMR of Al (0.4 nm)–Ni/SiO$_2$ and Al (4.0 nm)–Ni/SiO$_2$ after calcination: formation of aluminosilicates. To shed light onto the possible reaction between the ALD-grown Al_2O_3 layer and the SiO_2 support, the structure of calcined Al (4.0 nm)–Ni/SiO$_2$ was characterized by ^{27}Al MAS NMR and Raman spectroscopy (Fig. 3). Fig. 3a plots the ^{27}Al NMR spectra of the references α-Al_2O_3, γ-Al_2O_3, and a commercial amorphous aluminosilicate (Siral 70, 70 wt% of SiO_2). The ^{27}Al MAS NMR of the α-Al_2O_3 reference displays the expected signal for Al in an octahedral environment (Al^{VI}, δ = 9.0 ppm and C_Q = 2.5 MHz). The γ-Al_2O_3 reference for $NiAl_2O_4$ (structurally related) is composed primarily of Al^{IV}- (δ = 74 ppm and C_Q = 3.2 MHz) and Al^{VI}-coordinated Al sites (δ = 11 ppm and C_Q = 2.1 MHz) with a negligible amount of Al^V (δ = 40.3 ppm and C_Q = 4.2 MHz). For Siral 70, three types of Al sites, *i.e.*, Al^{IV} (δ = 57.8 ppm and C_Q = 4.3 MHz), Al^V (δ = 38.9 ppm and C_Q = 8.2 MHz), and Al^{VI} (δ = 6.7 ppm and C_Q = 1.9 MHz) are observed, which are in good agreement with previous NMR data of amorphous aluminosilicates (AAS).[58–60] Turning now to our catalysts, Fig. 3b plots the ^{27}Al NMR spectra of calcined (800 °C) Al (0.4 nm)–Ni/SiO$_2$ and Al (4.0 nm)–Ni/SiO$_2$. For calcined Al (0.4 nm)–Ni/SiO$_2$, three different Al sites are identified, *i.e.* Al^{IV} (δ = 63.4 ppm and C_Q = 8.5 MHz), Al^V (δ = 35.1 ppm and C_Q = 6.4 MHz) and Al^{VI} (δ = 9.1 ppm and C_Q = 5.8 MHz). Increasing the thickness of the ALD grown Al_2O_3 layer to 4.0 nm, *i.e.* calcined (800 °C) Al (4.0 nm)–Ni/SiO$_2$ similar ^{27}Al NMR resonance features are observed: Al^{IV} (δ = 59.0 ppm and C_Q = 4.6 MHz), Al^V (δ = 34.9 ppm and C_Q = 7.9 MHz) and Al^{VI} (δ = 5.7 ppm and C_Q = 2.6 MHz). The NMR features of Al (4.0 nm)–Ni/SiO$_2$, *i.e.* NMR shift (δ) and quadrupolar coupling constant (C_Q) of the different Al sites are similar to the values of Siral 70 and previously reported data on and Al_2O_3-rich AAS[59,60] and calcined (500 °C) ALD Al_2O_3-deposited SiO_2.[61] These NMR results point to a rearrangement of Al sites during calcination at 800 °C leading to the formation of AAS-like structures due to the reaction of Al_2O_3 with the SiO_2 support, *i.e.* the diffusion of Al atoms into the SiO_2 support, for both thicknesses of the ALD-grown Al_2O_3 layer studied here.

To probe more quantitatively the differences in the Al environment in calcined Al (0.4 nm)–Ni/SiO$_2$ and Al (4.0 nm)–Ni/SiO$_2$ the respective samples were exposed to an ammonia pretreatment. Previous reports have shown that ammonia treatment of AAS leads to the transformation of its Al^{VI} sites into Al^{IV} sites, whereas such a transformation (upon ammonia treatment) has not been observed for

γ-Al_2O_3.[59,60,62,63] In this context, we applied ammonia treatment to calcined Al (0.4 nm)–Ni/SiO$_2$ and Al (4.0 nm)–Ni/SiO$_2$, in order to probe the AAS content, following the hypothesis that only Al^{VI} sites in AAS will selectively transform into Al^{IV} sites by NH_3 treatment. Indeed, a comparison of the ^{27}Al NMR spectra of γ-Al_2O_3 before and after ammonia treatment (5 vol% NH_3/He at 120 °C for 5 h) features a negligible difference between the two spectra (Table S1 and Fig. S6a†), confirming previously reported observations.[59,60,62,63] On the other hand, for calcined Al (0.4 nm)–Ni/SiO$_2$ and Al (4.0 nm)–Ni/SiO$_2$, a transformation of Al^{VI} sites to Al^{IV} sites was observed after ammonia treatment (Fig. S6b† compared to Fig. 3b). The evaluated ratios of the Al^{IV}, Al^V, and Al^{VI} sites in Al (0.4 nm)–Ni/SiO$_2$ and Al (4.0 nm)–Ni/SiO$_2$ before and after ammonia treatment are summarized in Table S1.† After ammonia treatment the relative abundance of Al^{VI} sites in Al (0.4 nm)–Ni/SiO$_2$ and Al (4.0 nm)–Ni/SiO$_2$ decreased, while the relative abundance of Al^{IV} sites increased, providing further evidence of the presence of AAS in both materials.

To complement the ^{27}Al NMR studies, Raman spectroscopy was performed on calcined Al (0.4 nm)–Ni/SiO$_2$ and Al (4.0 nm)–N/SiO$_2$ (Fig. 3c). For bare Ni/SiO$_2$, a dominant band at 395 cm^{-1}, which is ascribed to Si–O–Si linkages in the tetrahedral unit of SiO_4, is observed.[64–66] In addition, the Si–O stretching band in the Si–O–Si plane is detected at 802 cm^{-1}. The bands at 483 cm^{-1} and 603 cm^{-1} are associate with the breathing modes of oxygen in, respectively, four (D1) and three (D2) membered rings of tetrahedral SiO_4.[67,68] An increase in the thickness of the ALD-grown Al_2O_3 layer leads to a reduction of the intensity of the Si–O–Si and SiO_4 bands, whereas new characteristic features appeared at 707 cm^{-1} and 1043 cm^{-1}. The band at 707 cm^{-1} is related to AlO_4 units and the band at 1043 cm^{-1} is attributed to Si–O–Al,[65,66,69] indicative of the presence of AAS in calcined Al (0.4 nm)–Ni/SiO$_2$ and Al (4.0 nm)–Ni/SiO$_2$. These findings are in good agreement with ^{27}Al NMR results. The intensified Si–O–Al band in Al (4.0 nm)–Ni/SiO$_2$ is due to its higher loading of Al, leading to a higher signal of the Raman band at 1043 cm^{-1}.

3.2.4. Acidic properties of calcined Al_2O_3-coated Ni/SiO$_2$ catalysts. The formation of amorphous aluminosilicates is expected to yield surface acid sites. To probe the presence of both Lewis and Brønsted acid sites, qualitative FTIR spectroscopy using pyridine as a probe molecule was performed (Fig. 4a). The FTIR transmittance spectra were collected after pyridine adsorption at 150 °C followed by outgassing at 150 °C under high vacuum conditions ($\approx$10^{-6} mbar) in order to remove adsorbed pyridine (Fig. 4a). The FTIR spectra of calcined Al (4.0 nm)–Ni/SiO$_2$ features both Brønsted and Lewis acid sites. The bands at 1450 cm^{-1} and 1610 cm^{-1} are ascribed to strong Lewis acid-bound pyridine, while the bands at 1550 cm^{-1} and 1640 cm^{-1} are attributed to pyridine protonated by Brønsted acid sites (pyridinium).[70,71] The band at 1492 cm^{-1} is assigned to physically adsorbed pyridine on both Brønsted and Lewis acid sites.[70,71] The

This journal is © The Royal Society of Chemistry 2021

Catal. Sci. Technol., 2021, **11**, 7563–7577 | 7569
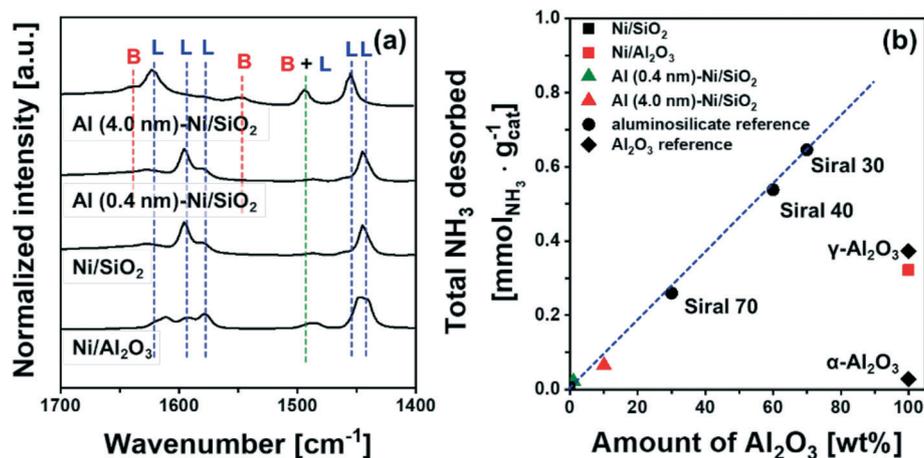
Fig. 4 Acidic properties: (a) difference FT-IR spectra of pyridine adsorbed on calcined Ni/SiO$_2$, Ni/Al$_2$O$_3$, Al (4.0 nm)–Ni/SiO$_2$ and the references α-Al$_2$O$_3$, γ-Al$_2$O$_3$, and Siral 70. The labels L and B mark Lewis and Brønsted acid sites, respectively. (b) The quantity of NH$_3$ desorbed during TPD as a function of the mass fraction of Al$_2$O$_3$.

reference α-Al$_2$O$_3$, γ-Al$_2$O$_3$ and Ni/Al$_2$O$_3$ exhibit Lewis acid sites whereas the commercial AAS catalyst Siral 70 showed both Lewis and Brønsted acid sites. Bare Ni/SiO$_2$ features only Lewis acid sites. The spectral features of calcined Al (0.4 nm)–Ni/SiO$_2$ are similar to Ni/SiO$_2$, showing predominantly Lewis acid sites whereas the presence of Brønsted acidity is observed in calcined Al (4.0 nm)–Ni/SiO$_2$. The Brønsted acidity in Al (4.0 nm)–Ni/SiO$_2$ is linked to the intensified Si–O–Al band as observed in its Raman spectrum.

To quantify the amount of acid sites, we performed NH$_3$-TPD (Fig. S7†). Bare Ni/SiO$_2$ and α-Al$_2$O$_3$ showed a negligible desorption of NH$_3$, i.e. 0.007 mmol NH$_3$ per g$_{cat}$ and 0.027 mmol NH$_3$ per g$_{cat}$, respectively. On the other hand, 0.373 mmol NH$_3$ per g$_{cat}$ and 0.322 mmol NH$_3$ per g$_{cat}$ were desorbed from γ-Al$_2$O$_3$ and bare Ni/Al$_2$O$_3$, attributed largely to Lewis acid sites. For commercial AAS, the quantity of desorbed NH$_3$ increases from 0.26 mmol NH$_3$ per g$_{cat}$ to 0.65 mmol NH$_3$ per g$_{cat}$ with an increase in the quantity of Al$_2$O$_3$ from 30 wt% (Siral 70) to 70 wt% (Siral 30). For the catalysts Al (0.4 nm)–Ni/SiO$_2$ and Al (4.0 nm)–Ni/SiO$_2$, the amount of NH$_3$ desorbed was 0.021 mmol NH$_3$ per g$_{cat}$ and 0.065 mmol NH$_3$ per g$_{cat}$, respectively. Overall, the amount of NH$_3$ desorbed showed a linear correlation with the amount Al$_2$O$_3$ in the AAS materials (Fig. 4b). Nevertheless, the amount of NH$_3$ desorbed from Al$_2$O$_3$-coated Ni/SiO$_2$ is small compared to γ-Al$_2$O$_3$ likely due to the amorphous nature of the Al$_2$O$_3$ layer.[72]

3.3. Catalyst activation: reduction of calcined Al$_2$O$_3$-coated Ni/SiO$_2$ catalysts

The reduction behavior of the calcined Al$_2$O$_3$-coated Ni/SiO$_2$ catalysts was assessed by H$_2$-TPR (Fig. 5a). The reducible Ni^{2+} species can be classified as: (i) α-type (weak interaction with support, 290–475 °C), (ii) β-type (mid-interaction with support, 475–753 °C), and (iii) γ-type (strong interaction with support, 753–894 °C).[73–76] As references we used commercial

NiO, NiAl$_2$O$_4$, Ni impregnated on Siral 70 and Ni impregnated on Al$_2$O$_3$-coated SiO$_2$ (Ni/Al (4.0 nm)–SiO$_2$). The TPR profiles of the NiO and NiAl$_2$O$_4$ references showed a reduction peak at 415 °C and 803 °C, respectively, corresponding to α- and γ-type reduction behaviors. Ni/Siral 70 and Ni/Al (4.0 nm)–SiO$_2$ calcined at 800 °C revealed a reduction peak at 611 °C and 617 °C, respectively, indicative of a β-type reduction. The β-type reduction is ascribed to an interaction of NiO with alumina (NiO–Al$_2$O$_3$). This observation suggests that the formation of AAS mitigates the further reaction of NiO with Al$_2$O$_3$ (forming NiAl$_2$O$_4$); however, the interaction of NiO with Al$_2$O$_3$ leads to a higher reduction temperature compared to bulk NiO.[73,77–79] H$_2$-TPR of Ni/SiO$_2$ revealed a low reduction temperature of 450 °C indicative of a weak Ni–silica interaction, in agreement with literature.[80,81] On the other hand, two reduction peaks were observed in the H$_2$-TPR of Al (0.4 nm)–Ni/SiO$_2$ and Al (4.0 nm)–Ni/SiO$_2$. In Al (0.4 nm)–Ni/SiO$_2$ the reduction peaks at 450 °C and 600 °C are attributed to the reduction of NiO interacting with SiO$_2$ and free Al$_2$O$_3$. Increasing the thickness of the ALD-grown Al$_2$O$_3$ layer, i.e., Al (4.0 nm)–Ni/SiO$_2$, leads to reduction temperatures of 600 °C and 800 °C owing to the interaction of NiO with free Al$_2$O$_3$ on Al (4.0 nm)–Ni/SiO$_2$, and the reaction of NiO with Al$_2$O$_3$ forming NiAl$_2$O$_4$, respectively.

In the following, we utilize in situ XANES at the Ni K-edge (Fig. 5b) and in situ XRD (Fig. S8b†) during reduction to probe in more detail the reduction pathway of Ni^{2+} species in the calcined catalysts. Calcined Ni/SiO$_2$ (α-type Ni^{2+}) and Al (4.0 nm)–Ni/SiO$_2$ (β- and γ-type Ni^{2+}) were chosen for in situ XAS–XRD experiments as they show the largest difference in the H$_2$-TPR experiments (whereby Al (0.4 nm)–Ni/SiO$_2$ can be considered, from a reduction behavior perspective, as a mixture of Ni/SiO$_2$ (α-type Ni^{2+}) and Al (4.0 nm)–Ni/SiO$_2$ (β- and γ-type Ni^{2+}) features). For bare Ni/SiO$_2$, in situ XANES revealed that the reduction of NiO started at 250 °C; NiO was fully reduced to metallic Ni at 450 °C. The appearance of (111), (200) and (220) reflections due to Ni^0 (fcc) in the in situ

7570 | Catal. Sci. Technol., 2021, **11**, 7563–7577

This journal is © The Royal Society of Chemistry 2021
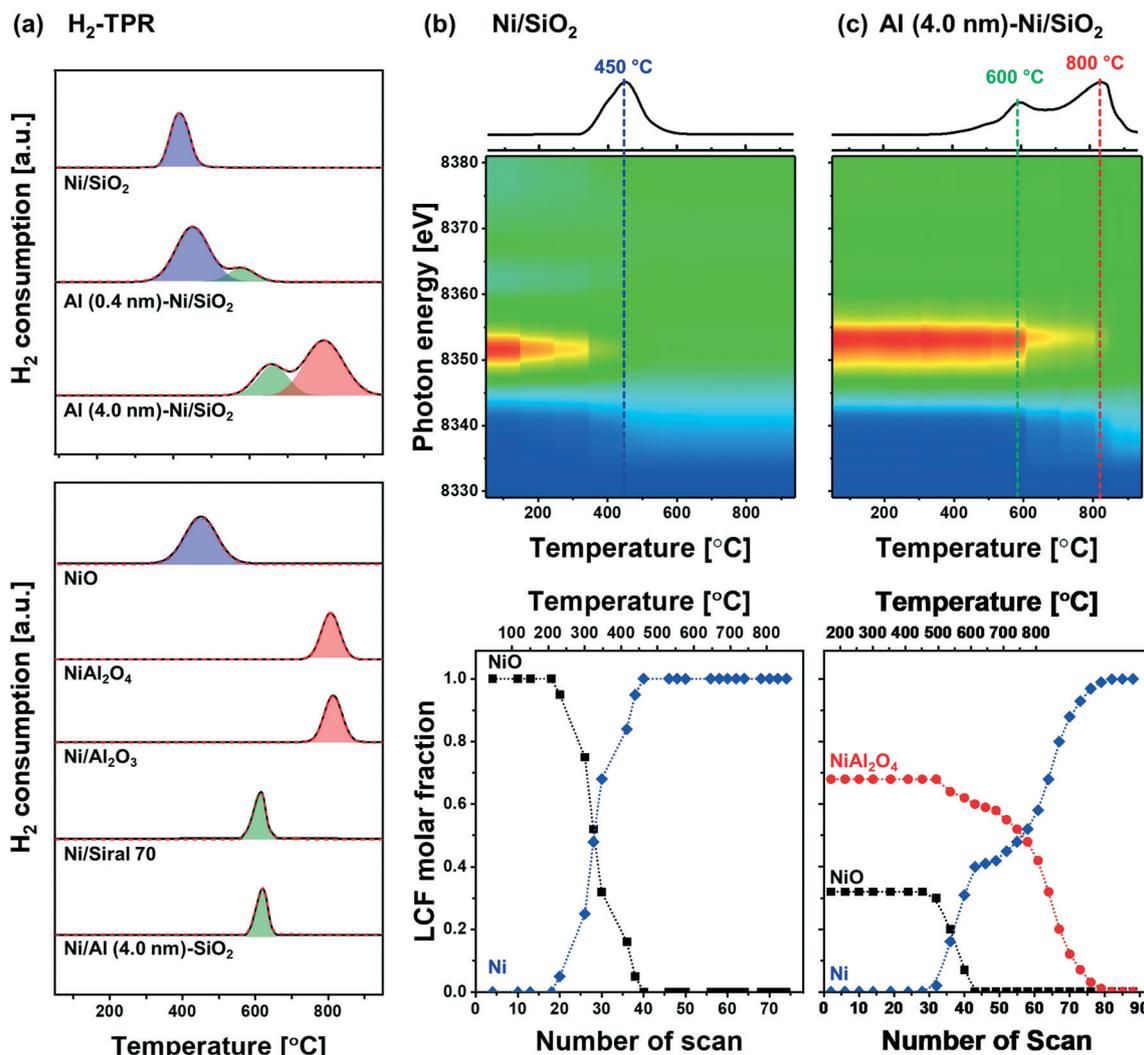
Fig. 5 Characterization of the reduced materials: (a) H_2-TPR of the references (NiO, Ni/Al_2O_4, Ni/Al_2O_3 and $Ni/Siral$ 70) and calcined Ni/SiO_2, Al (0.4 nm)–Ni/SiO_2 and Al (4.0 nm)–Ni/SiO_2. Contour plots of the acquired *in situ* Ni K-edge XANES data and the corresponding LCF analysis of (b) Ni/SiO_2 and (c) Al (4.0 nm)–Ni/SiO_2 during reduction.

XRD data at temperatures exceeding 300 °C is indicative of the formation of metallic Ni through the direct reduction of bulk NiO (Fig. S8a†). LCF analysis of the XANES data of calcined Al (4.0 nm)–Ni/SiO_2 yielded a composition of 32 mol% NiO and 68 mol% $NiAl_2O_4$. LCF of the *in situ* XANES and XRD showed that in calcined Al (4.0 nm)–Ni/SiO_2, NiO was reduced in the temperature range 500–600 °C, whereas $NiAl_2O_4$ was reduced between 550 °C and 800 °C.

To summarize, combining our insight of the structure of calcined Al (0.4 nm)–Ni/SiO_2 and Al (4.0 nm)–Ni/SiO_2 with its reduction behavior, we can deduce that the reduction occurring at 400 °C is ascribed to the reduction of NiO weakly interacting with SiO_2, whereas NiO interacting with free Al_2O_3 in Al_2O_3-modified SiO_2, *i.e.*, AAS, reduces only at 600 °C. In addition, the availability of excessive, free Al_2O_3 domains in Al (4.0 nm)–Ni/SiO_2 results in the formation of $NiAl_2O_4$ (NiO + Al_2O_3 → $NiAl_2O_4$) which reduces at 800 °C. ^{27}Al NMR measurements of the reduced materials revealed no

significant differences to the calcined material (Fig. S6c†), indicating that AAS remains as such in the catalysts after reduction. Overall, our structural characterization using XRD, XAS, Raman and ^{27}Al NMR point to the formation of both AAS, and $NiAl_2O_4$ in Al_2O_3-coated Ni/SiO_2 catalysts.

Electron microscopy of reduced Al (4.0 nm)–Ni/SiO_2 was performed to visualize the morphology of the Ni nanoparticles and the ALD-grown Al_2O_3 layer (Fig. 6). HR-TEM of reduced Al (4.0 nm)–Ni/SiO_2 (Fig. 6a) shows metallic Ni nanoparticles with a size of 8 ± 1 nm. The Ni nanoparticles were partly embedded in the support and partly covered by an amorphous (ALD-grown) layer. Hence, increasing the thickness of the ALD-grown Al_2O_3 layer from 0.4 nm to 4.0 nm, will reduce the number of active (and accessible) active Ni active sites at the surface, which is in line with a decrease in the quantity of chemisorbed H_2 with increasing thickness of the ALD-grown Al_2O_3 layer, as tabulated in Table 1. The mean Ni particle size determined

This journal is © The Royal Society of Chemistry 2021

Catal. Sci. Technol., 2021, **11**, 7563–7577 | **7571**
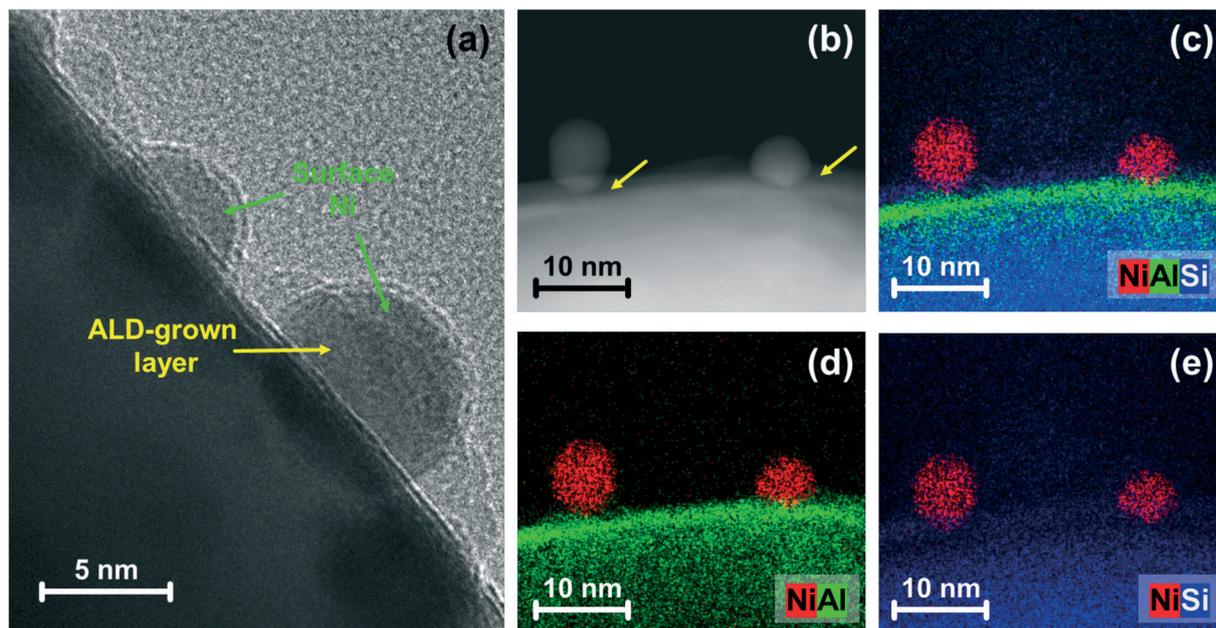
Fig. 6 Electron microscopy-based morphological characterization: (a) HR-TEM and (b) HAADF-STEM images with (c–e) EDX mapping for reduced Al (4.0 nm)–Ni/SiO₂. The arrows represent the ALD-grown layer.

by H₂ chemisorption using a hemisphere model is larger than the TEM-estimated Ni particle size. This difference is ascribed to the partial covering of the Ni surface by the Al₂O₃ overcoat.

To probe further the morphology and composition of the Al₂O₃ layer, STEM images combined with elemental EDX analysis (Fig. 6b–e and S9†) of reduced Al (4.0 nm)–Ni/SiO₂ were acquired. At the top of the silica spheres, an Al-containing layer forms. The overlap of the signals from Si and Al are indicative of a reaction between SiO₂ and Al₂O₃. The particle size of Ni after reduction, as determined by TEM (Fig. S4† and Table 1) was similar for all of the reduced catalysts: Ni/SiO₂ (7 ± 2 nm), Al (0.4 nm)–Ni/SiO₂ (7 ± 2 nm) and Al (4.0 nm)–Ni/SiO₂ (8 ± 1 nm). However, the amount of surface Ni of the reduced catalysts, quantified by H₂ chemisorption using a stoichiometry factor of H/Ni = 1 (ref. 48 and 50) decreased with increasing thickness of the ALD-grown Al₂O₃ layer, i.e., 102 μmol_Ni g_cat⁻¹ (Ni/SiO₂) > 91 μmol_Ni g_cat⁻¹ (Al (0.4 nm)–Ni/SiO₂) > 70 μmol_Ni g_cat⁻¹ (Al (4.0 nm)–Ni/SiO₂). This observation can be explained by the partial coverage of surface Ni by the ALD-grown Al₂O₃ layer.

3.4. Dry reforming of methane activity and selectivity

The catalytic activity tests for DRM were performed in a fixed-bed quartz reactor. In a typical experiment, prior to the activity test, the respective calcined catalysts were first reduced (based on the TPR results) at 400 °C (Ni/SiO₂), 600 °C (Al (0.4 nm)–Ni/SiO₂), and 800 °C (Ni/Al₂O₃ and Al (4.0 nm)–Ni/SiO₂) in 10 vol% H₂/N₂ (100 ml min⁻¹) for 2 h. The DRM performance was evaluated in the kinetic regime, i.e., far from the equilibrium conversion of methane, at 700 °C

using a GHSV of 300 L g_cat⁻¹ h⁻¹ (100 mL min⁻¹ of 45% CH₄, 45% CO₂ and 10% N₂). The DRM performances of the Al₂O₃-coated Ni/SiO₂ based catalysts (Al (0.4 nm)–Ni/SiO₂ and Al (4.0 nm)–Ni/SiO₂) were compared with the following benchmark catalysts: (i) Ni supported on SiO₂ or Al₂O₃ (Ni/SiO₂ and Ni/Al₂O₃), (ii) Ni supported on Al₂O₃-coated SiO₂ (Ni/Al (4.0 nm)–SiO₂) and Ni supported on Al₂O₃-coated Al₂O₃ (Ni/Al (4.0 nm)–Al₂O₃) and (iii) Al₂O₃-coated Ni/Al₂O₃ (Al (0.4 nm)–Al₂O₃).

As expected, we observe severe deactivation for Ni/SiO₂, exhibiting a drastic reduction of the methane consumption rate with TOS, i.e., from 33 mmol_CH₄ min⁻¹ g_cat⁻¹ to 5 mmol_CH₄ min⁻¹ g_cat⁻¹ after 10 h TOS (Fig. 7a). A gradual decrease of the methane consumption rate was also observed for Ni/Al₂O₃ (from 27 mmol_CH₄ min⁻¹ g_cat⁻¹ to 20 mmol_CH₄ min⁻¹ g_cat⁻¹), Ni/Al (4.0 nm)–SiO₂ (from 38 mmol_CH₄ min⁻¹ g_cat⁻¹ to 30 mmol_CH₄ min⁻¹ g_cat⁻¹) and Ni/Al (4.0 nm)–Al₂O₃ (from 30 mmol_CH₄ min⁻¹ g_cat⁻¹ to 26 mmol_CH₄ min⁻¹ g_cat⁻¹). These results show that the deactivation tendency of Ni catalysts when impregnated onto Al₂O₃ (Ni/Al₂O₃) and Al₂O₃-coated supports (Ni/Al (4.0 nm)–SiO₂ and Ni/Al (4.0 nm)–Al₂O₃) improves only partially.

Turning now to the catalysts for which the Al₂O₃ overcoat was deposited after Ni impregnation onto the SiO₂ support, the methane consumption rate at 1 h of TOS of Al (0.4 nm)–Ni/SiO₂ (30 mmol_CH₄ min⁻¹ g_cat⁻¹) Al (4.0 nm)–Ni/SiO₂ (23 mmol_CH₄ min⁻¹ g_cat⁻¹) and Al (4.0 nm)–Ni/Al₂O₃ (18 mmol_CH₄ min⁻¹ g_cat⁻¹) are reduced compared to the corresponding benchmarks Ni/SiO₂ and Ni/Al₂O₃ (Fig. 7a and b). After 10 h of TOS, the methane consumption rate of Al (0.4 nm)–Ni/SiO₂ has reduced to 20 mmol_CH₄ min⁻¹ g_cat⁻¹, while a very stable methane consumption rate was observed for Al (4.0 nm)–Ni/

7572 | Catal. Sci. Technol., 2021, **11**, 7563–7577

This journal is © The Royal Society of Chemistry 2021
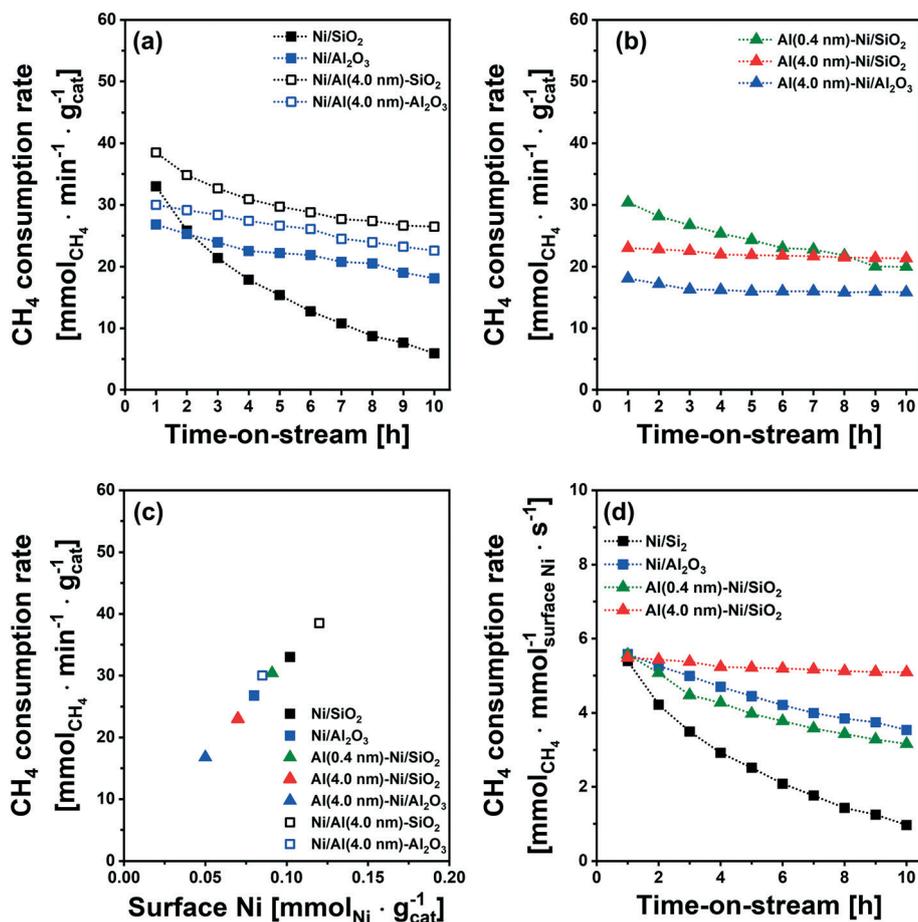
Fig. 7 DRM performance: rate of methane consumption for (a) Ni supported on bare SiO_2 and Al_2O_3-coated SiO_2 and Al_2O_3, and (b) Al_2O_3-coated Ni/SiO_2 and Ni/Al_2O_3 as a function of TOS, (c) rate of methane consumption at 1 h of TOS as a function of surface Ni as quantified by H_2 chemisorption (H/Ni = 1.0), and (d) rate of methane consumption normalized by surface Ni of the freshly reduced catalysts, quantified by H_2 chemisorption (H/Ni = 1.0), as a function of TOS.

SiO_2 (23 $mmol_{CH_4}$ min^{-1} g_{cat}^{-1} over 10 h TOS). For Al (4.0 nm)–Ni/Al_2O_3 the initial methane consumption rate (1 h TOS) was reduced from 18 $mmol_{CH_4}$ min^{-1} g_{cat}^{-1} to 16 $mmol_{CH_4}$ min^{-1} g_{cat}^{-1} after 2 h of TOS, but remained stable at 16 $mmol_{CH_4}$ min^{-1} g_{cat}^{-1}) at 10 h TOS. These findings show that an Al_2O_3 overcoat of a thickness of 4 nm deposited onto Ni/SiO_2 or Ni/Al_2O_3 is effective to stabilize the DRM performance of the impregnated Ni catalysts. The inverse preparation route, *i.e.*, the impregnation of Ni onto Al_2O_3-coated SiO_2 and Al_2O_3 supports did not yield stable catalysts.

It is important to note that the initial methane consumption rate (normalized by weight catalyst) decreases with increasing thickness of the Al_2O_3 overcoats. This is ascribed to (i) the reduced Ni content per mass catalyst and (ii) the reducing number of accessible active surface Ni sites (H_2 chemisorption data, Table 1) with an increasing quantity of Al_2O_3 deposited. Fig. 7c confirms that there is a linear correlation between the methane consumption rate (1 h of TOS) with surface Ni, as quantified by H_2 chemisorption (H/Ni = 1.0), providing further evidence that surface metallic Ni is the active site for DRM. The methane consumption rate (1 h of TOS) normalized by surface Ni (Fig. 7d) features very

similar values (5.4–5.7 $mmol_{CH4}$ $mmol_{surface\ Ni}^{-1}$ s^{-1}) for Ni/SiO_2, Ni/Al_2O_3, Al (0.4 nm)–Ni/SiO_2 and Al (4.0 nm)–Ni/SiO_2.

3.5. Structure–stability relationship: Al_2O_3 overcoat stabilizing the catalyst against coking and sintering

To obtain further insight into the enhanced stability of Al (4.0 nm)–Ni/SiO_2 when compared to the uncoated benchmark catalysts (*i.e.*, Ni/SiO_2 and Ni/Al_2O_3), additional *in situ* and post-reaction analyses were performed.

In situ XRD data acquired during the DRM at 700 °C (Fig. 8a) revealed a noticeable (002) reflection due to graphitic carbon (space group $P6_3/mmc$) for Ni/SiO_2 and Ni/Al_2O_3 after 5 h of TOS. On the other hand, no crystalline carbon was detected for Al (4.0 nm)–Ni/SiO_2, implying that graphite C formation was at least one of the reasons leading to the deactivation of uncoated Ni/SiO_2 and Ni/Al_2O_3. For Ni/Al_2O_3 *in situ* XRD also reveals a decrease in the intensity of the Ni^0 peaks (with respect to the intensity of the support), likely due to the formation of $NiAl_2O_4$. However, due to overlapping diffraction peaks the distinction between spinel γ-Al_2O_3 and $NiAl_2O_4$ is difficult. Thus, the *in situ* XRD study
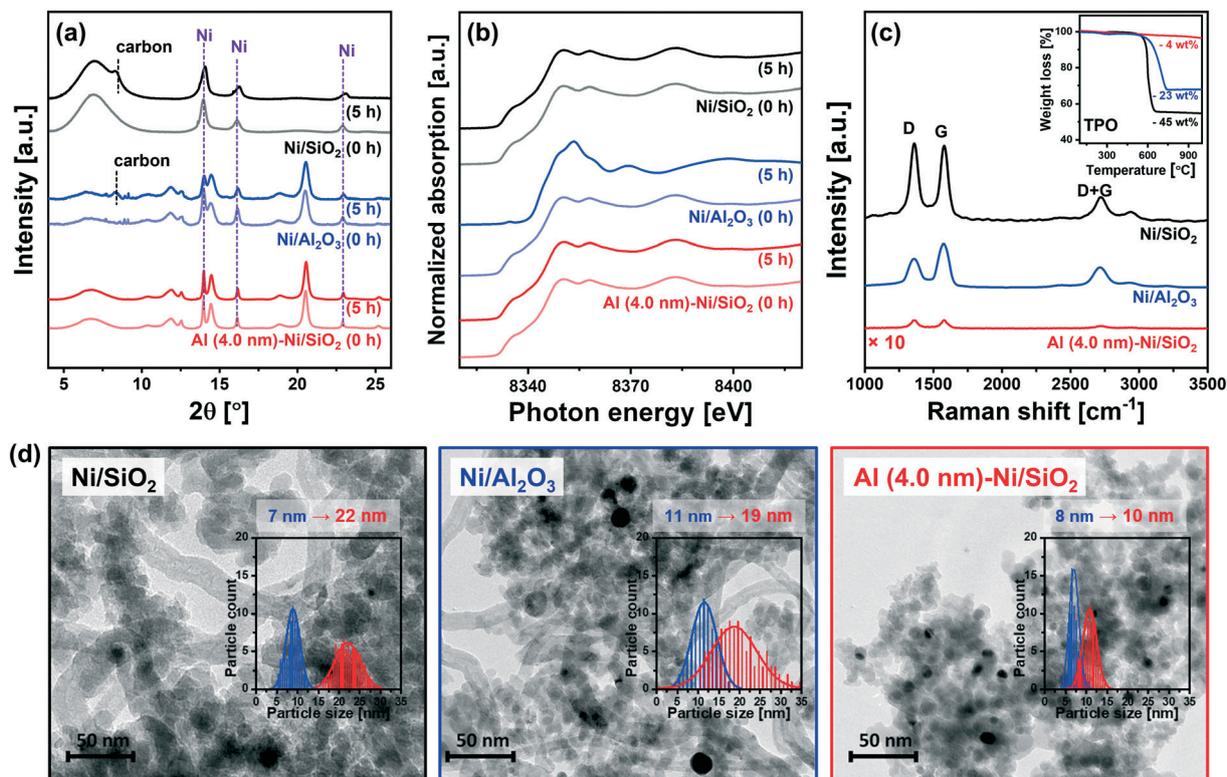
Fig. 8 Morphological and structural characterization of the spent catalysts: Selected *in situ* (a) diffractograms and (b) Ni K-edge XANES acquired under DRM conditions and (c) Raman spectra of spent Ni/SiO₂, Ni/Al₂O₃ and Al (4.0 nm)–Ni/SiO₂. The asterisk in (a) represents γ-Al₂O₃ (ICSD 66559) or NiAl₂O₄ (ICSD 9554). The inset in (b) plots the weight loss of the spent catalysts as a function of temperature during a TPO experiment. (d) TEM images and Ni particle size distribution of the spent catalyst.

was complemented by XAS characterization of the post-reaction catalysts to determine the oxidation state of Ni. To examine the oxidation state of Ni in the catalyst materials, *in situ* and *ex situ* XANES spectra at the Ni K-edge after 5 h and 10 h of DRM were collected (Fig. 8b and S10†). It should be noted that all of the catalysts were completely reduced to metallic Ni^0 prior to DRM, *i.e.*, TOS = 0 h. The *in situ* Ni K-edge XANES data (Fig. 8b) does not show significant changes in the oxidation state of Ni for Ni/SiO₂ and Al (4.0 nm)–Ni/SiO₂ after 5 h of DRM. On the other hand, the XANES spectra of spent Ni/Al₂O₃ showed a partial oxidation of metallic Ni forming NiAl₂O₄. The oxidation of metallic Ni to NiAl₂O₄ was also observed for Ni/Al (4.0 nm)–Al₂O₃ and Al (4.0 nm)–Ni/Al₂O₃ (Fig. S10†). From a LCF analysis of the *ex situ* XANES data we quantified that 10, 10 and 9 mol% of Ni in Ni/Al₂O₃, Ni/Al (4.0 nm)–Al₂O₃ and Al (4.0 nm)–Ni/Al₂O₃ were converted into NiAl₂O₄ during 10 h of DRM (Table S2†). The migration of Ni^0 into the Al₂O₃ lattice forming NiAl₂O₄ can explain (with carbon deposition) the deactivation of these three catalysts. Importantly, we did not observe any Ni oxidation in spent Al (4.0 nm)–Ni/SiO₂ and Ni/Al (4.0 nm)–SiO₂, *i.e.* Ni was maintained in its metallic form over 10 h of TOS. These peculiar results of the Al₂O₃-ALD/SiO₂-based catalysts are possibly due to the presence of aluminosilicates in Al (4.0 nm)–Ni/SiO₂ and Ni/Al (4.0 nm)–SiO₂ that prevent the formation of NiAl₂O₄. Hence, the presence of

aluminosilicates resulting from the interaction of the ALD-grown Al₂O₃ layer with SiO₂ upon calcination seems to mitigate the migration (and oxidation) of Ni into the Al₂O₃ matrix.

The quantity of the carbon deposited was determined by temperature programmed oxidation (TPO) on the spent catalysts that were collected after the *in situ* XAS–XRD measurements under DRM conditions for 5 h (inset in Fig. 8c). The weight increase in the temperature range of 300–450 °C is mostly due to the oxidation of Ni to NiO. The weight loss due to the oxidation of deposited carbon species occurs at 600 °C for Ni/SiO₂ and Al (4.0 nm)–Ni/SiO₂, and at 715 °C for Ni/Al₂O₃. The quantity of deposited carbon followed the order: Ni/SiO₂ (45 wt%) > Ni/Al₂O₃ (23 wt%) ≫ Al (4.0 nm)–Ni/SiO₂ (4 wt%).

Raman spectra of all of the spent catalysts showed characteristic D and G bands of carbon at 1250–1350 cm⁻¹ and 1500–1700 cm⁻¹, respectively (Fig. 8c). The D bands represent disordered carbon species, *e.g.*, amorphous or defective filamentous carbon, whereas the G band represents the stretching mode of the sp² bonds in ordered graphite.[82,83] The very low intensity of the peaks in the Raman spectra for Al (4.0 nm)–Ni/SiO₂ is in line with the quantitative carbon analysis using TPO, *i.e.* very little carbon deposition on spent Al (4.0 nm)–Ni/SiO₂ compared to spent Ni/SiO₂ and Ni/Al₂O₃. The ratio of the intensities of the G and D bands (I_G/I_D)

7574 | *Catal. Sci. Technol.*, 2021, **11**, 7563–7577

This journal is © The Royal Society of Chemistry 2021

provides an indication on the degree of crystallinity of the deposited carbon,[84] whereby a high ratio of I_G/I_D points to a high crystallinity. For spent Ni/Al$_2$O$_3$ I_G/I_D = 1.3, which is higher than the values for spent Ni/SiO$_2$ (I_G/I_D = 1.0) and Al (4.0 nm)–Ni/SiO$_2$ (I_G/I_D = 1.0). The crystallinity of the carbon deposited affects the oxidation temperature of carbon, i.e., an increasing oxidation temperature with an increasing degree of carbon crystallinity.[9] Hence our findings concerning the I_G/I_D values for the different catalysts are in line with the higher oxidation temperature of carbon deposited onto Ni/Al$_2$O$_3$ (715 °C) compared to Ni/SiO$_2$ and Al (4.0 nm)–Ni/SiO$_2$ (600 °C). These results confirm that the significant deposition of coke is a key reason for the deactivation of the uncoated catalysts, i.e. Ni/SiO$_2$ and Ni/Al$_2$O$_3$, whereas Al (4.0 nm)–Ni/SiO$_2$ shows a very high resistance to coke formation. An increasing degree of coke formation during DRM can be explained by the following factors: (i) surface acidity of the catalyst support (basic sites can alleviate coke deposition by promoting the oxidation of surface carbon[85]) and (ii) sintering of Ni particles. Considering the observed trends in coke formation, particle size and acidity, we ascribe the main driver to coke formation in our set of model catalysts to differences in the growth of the Ni particle size during DRM. Coke formation and particle growth were also visualized by TEM. The formation of filamentous carbon on spent Ni/SiO$_2$ and Ni/Al$_2$O$_3$ was observed, whereas no coke formation was revealed in the TEM images of spent Al (4.0 nm)–Ni/SiO$_2$ (Fig. 8d). Measuring the particle growth during DRM through the analysis of TEM images, a 3.1-fold (from 7 nm to 22 nm) and 1.7-fold (from 11 nm to 19 nm) increase in the Ni particle size was observed for Ni/SiO$_2$ and Ni/Al$_2$O$_3$, respectively. On the other hand, a significantly reduced increase in the particle size of Ni (from 8 nm to 10 nm, i.e., 25%) was observed for Al (4.0 nm)–Ni/SiO$_2$, demonstrating the stabilizing effect of an ALD-grown overcoat of Al$_2$O$_3$ on the Ni nanoparticles, preventing in turn their sintering during DRM.

To summarize our detailed characterization of the as-prepared and spent catalysts attribute the remarkable stability of Al (4.0 nm)–Ni/SiO$_2$ during DRM to (i) the confinement of Ni nanoparticles by the Al$_2$O$_3$ overcoat preventing coke deposition on edge and step sites in large Ni particles, and (ii) the formation of aluminosilicates that mitigate the migration and oxidation of Ni preventing NiAl$_2$O$_4$ formation.

4. Conclusions

We have developed stable Ni-based DRM catalysts by employing atomic layer deposition (ALD) to ensure the deposition of a conformal layer of Al$_2$O$_3$ onto Ni nanoparticles supported on SiO$_2$. Al$_2$O$_3$-coated Ni/SiO$_2$ that showed a remarkable DRM stability when compared to the benchmark references Ni/SiO$_2$ and Ni/Al$_2$O$_3$. An in-depth structural characterization of the Al$_2$O$_3$-coated catalysts and several benchmark systems via in situ Ni K-edge XAS–XRD

complemented by H$_2$-TPR and solid-state ^{27}Al NMR revealed the reaction of the ALD-grown Al$_2$O$_3$ layer with the SiO$_2$ support and Ni during calcination, i.e., forming an aluminosilicate and NiAl$_2$O$_4$, respectively. The deactivation of the uncoated benchmark catalysts, i.e., Ni/Al$_2$O$_3$ and Ni/SiO$_2$, is ascribed to Ni particle growth and coke formation during DRM. An additional deactivation route of the Ni/Al$_2$O$_3$ benchmark is the migration/oxidation of Ni into the Al$_2$O$_3$ matrix forming (inactive) NiAl$_2$O$_3$. The best catalyst prepared, i.e. Al (4.0 nm)–Ni/SiO$_2$, showed a remarkable stability (maintenance of 89% of the initial methane consumption rate after 10 h of TOS) under DRM conditions owing to the confinement of Ni nanoparticles by the Al$_2$O$_3$ overcoat and the inhibition of the oxidation of Ni and reaction with Al$_2$O$_3$ in the presence of aluminosilicates.

Conflicts of interest

The authors declare no competing financial interest.

References

1 A. Otto, T. Grube, S. Schiebahn and D. Stolten, Energy Environ. Sci., 2015, 8, 3283–3297.
2 J. C. Abanades, E. S. Rubin, M. Mazzotti and H. J. Herzog, Energy Environ. Sci., 2017, 10, 2491–2499.
3 I. Dimitriou, P. García-Gutiérrez, R. H. Elder, R. M. Cuéllar-Franca, A. Azapagic and R. W. K. Allen, Energy Environ. Sci., 2015, 8, 1775–1789.
4 P. Markewitz, W. Kuckshinrichs, W. Leitner, J. Linssen, P. Zapp, R. Bongartz, A. Schreiber and T. E. Muller, Energy Environ. Sci., 2012, 5, 7281–7305.
5 S. M. Kim, P. M. Abdala, M. Broda, D. Hosseini, C. Copéret and C. Müller, ACS Catal., 2018, 8, 2815–2823.
6 R. L. Espinoza, A. P. Steynberg, B. Jager and A. C. Vosloo, Appl. Catal., A, 1999, 186, 13–26.
7 A. P. Steynberg, R. L. Espinoza, B. Jager and A. C. Vosloo, Appl. Catal., A, 1999, 186, 41–54.
8 J. R. Rostrupnielsen and J. H. B. Hansen, J. Catal., 1993, 144, 38–49.

9 S. M. Kim, P. M. Abdala, T. Margossian, D. Hosseini, L. Foppa, A. Armutlulu, W. van Beek, A. Comas-Vives, C. Copéret and C. Müller, *J. Am. Chem. Soc.*, 2017, **139**, 1937–1949.

10 T. Margossian, K. Larmier, S. M. Kim, F. Krumeich, C. Müller and C. Copéret, *ACS Catal.*, 2017, **7**, 6942–6948.

11 T. Margossian, K. Larmier, S. M. Kim, F. Krumeich, A. Fedorov, P. Chen, C. R. Müller and C. Copéret, *J. Am. Chem. Soc.*, 2017, **139**, 6919–6927.

12 S. M. Kim, A. Armutlulu, A. M. Kierzkowska, D. Hosseini, F. Donat and C. Müller, *Sustainable Energy Fuels*, 2020, **4**, 713–729.

13 J. W. Han, C. Kim, J. S. Park and H. Lee, *ChemSusChem*, 2014, **7**, 451–456.

14 J.-H. Kim, D. J. Suh, T.-J. Park and K.-L. Kim, *Appl. Catal., A*, 2000, **197**, 191–200.

15 S. Kawi, Y. Kathiraser, J. Ni, U. Oemar, Z. Li and E. T. Saw, *ChemSusChem*, 2015, **8**, 3556–3575.

16 A. Tsoukalou, Q. Imtiaz, S. M. Kim, P. M. Abdala, S. Yoon and C. R. Müller, *J. Catal.*, 2016, **343**, 208–214.

17 D. L. Trimm, *Catal. Today*, 1999, **49**, 3–10.

18 A. J. van Dillen, R. J. A. M. Terörde, D. J. Lensveld, J. W. Geus and K. P. de Jong, *J. Catal.*, 2003, **216**, 257–264.

19 L. Xu, H. Song and L. Chou, *ACS Catal.*, 2012, **2**, 1331–1342.

20 D. M. Argyle and H. C. Bartholomew, *Catalysts*, 2015, **5**, 145–269.

21 M. Akri, S. Zhao, X. Li, K. Zang, A. F. Lee, M. A. Isaacs, W. Xi, Y. Gangarajula, J. Luo, Y. Ren, Y.-T. Cui, L. Li, Y. Su, X. Pan, W. Wen, Y. Pan, K. Wilson, L. Li, B. Qiao, H. Ishii, Y.-F. Liao, A. Wang, X. Wang and T. Zhang, *Nat. Commun.*, 2019, **10**, 5181.

22 D. Baudouin, U. Rodemerck, F. Krumeich, A. D. Mallmann, K. C. Szeto, H. Ménard, L. Veyre, J.-P. Candy, P. B. Webb, C. Thieuleux and C. Copéret, *J. Catal.*, 2013, **297**, 27–34.

23 J. A. Lercher, J. H. Bitter, W. Hally, W. Niessen and K. Seshan, in *Stud. Surf. Sci. Catal.*, ed. J. W. Hightower, W. Nicholas Delgass, E. Iglesia and A. T. Bell, Elsevier, 1996, vol. 101, pp. 463–472.

24 S. Tang, L. Ji, J. Lin, H. C. Zeng, K. L. Tan and K. Li, *J. Catal.*, 2000, **194**, 424–430.

25 D. Baudouin, K. C. Szeto, P. Laurent, A. De Mallmann, B. Fenet, L. Veyre, U. Rodemerck, C. Copéret and C. Thieuleux, *J. Am. Chem. Soc.*, 2012, **134**, 20624–20627.

26 P. Littlewood, S. Liu, E. Weitz, T. J. Marks and P. C. Stair, *Catal. Today*, 2020, **343**, 18–25.

27 J. W. Han, J. S. Park, M. S. Choi and H. Lee, *Appl. Catal., B*, 2017, **203**, 625–632.

28 C. Wang, H. Wang, Q. Yao, H. Yan, J. Li and J. Lu, *J. Phys. Chem. C*, 2016, **120**, 478–486.

29 T. M. Onn, S. Zhang, L. Arroyo-Ramirez, Y.-C. Chung, G. W. Graham, X. Pan and R. J. Gorte, *ACS Catal.*, 2015, **5**, 5696–5701.

30 J. Lu, B. Fu, M. C. Kung, G. Xiao, J. W. Elam, H. H. Kung and P. C. Stair, *Science*, 2012, **335**, 1205.

31 E. Baktash, P. Littlewood, R. Schomäcker, A. Thomas and P. C. Stair, *Appl. Catal., B*, 2015, **179**, 122–127.

32 Y. Lou, M. Steib, Q. Zhang, K. Tiefenbacher, A. Horváth, A. Jentys, Y. Liu and J. A. Lercher, *J. Catal.*, 2017, **356**, 147–156.

33 S. Wang and G. Q. Lu, *J. Chem. Technol. Biotechnol.*, 2000, **75**, 589–595.

34 J. Juan-Juan, M. C. Román-Martínez and M. J. Illán-Gómez, *Appl. Catal., A*, 2006, **301**, 9–15.

35 D. La Rosa, A. Sin, M. L. Faro, G. Monforte, V. Antonucci and A. S. Aricò, *J. Power Sources*, 2009, **193**, 160–164.

36 M. H. Amin, S. Putla, S. Bee Abd Hamid and S. K. Bhargava, *Appl. Catal., A*, 2015, **492**, 160–168.

37 Z. Bian, S. Das, M. H. Wai, P. Hongmanorom and S. Kawi, *ChemPhysChem*, 2017, **18**, 3117–3134.

38 B. Steinhauer, M. R. Kasireddy, J. Radnik and A. Martin, *Appl. Catal., A*, 2009, **366**, 333–341.

39 B. Pawelec, S. Damyanova, K. Arishtirova, J. L. G. Fierro and L. Petrov, *Appl. Catal., A*, 2007, **323**, 188–201.

40 Z. Hou and T. Yashima, *Catal. Lett.*, 2003, **89**, 193–197.

41 C. Crisafulli, S. Scirè, R. Maggiore, S. Minicò and S. Galvagno, *Catal. Lett.*, 1999, **59**, 21–26.

42 P. Djinović, I. G. Osojnik Črnivec, B. Erjavec and A. Pintar, *Appl. Catal., B*, 2012, **125**, 259–270.

43 J. Zhang, H. Wang and A. K. Dalai, *J. Catal.*, 2007, **249**, 300–310.

44 N. Rahemi, M. Haghighi, A. A. Babaluo, M. F. Jafari and S. Khorram, *Int. J. Hydrogen Energy*, 2013, **38**, 16048–16061.

45 S. J. Tauster, *Acc. Chem. Res.*, 1987, **20**, 389–394.

46 B. J. O'Neill, D. H. K. Jackson, J. Lee, C. Canlas, P. C. Stair, C. L. Marshall, J. W. Elam, T. F. Kuech, J. A. Dumesic and G. W. Huber, *ACS Catal.*, 2015, **5**, 1804–1825.

47 S. M. Maier, A. Jentys and J. A. Lercher, *J. Phys. Chem. C*, 2011, **115**, 8005–8013.

48 C. H. Bartholomew, *Catal. Lett.*, 1990, **7**, 27–51.

49 C. H. Bartholomew, R. B. Pannell and J. L. Butler, *J. Catal.*, 1980, **65**, 335–347.

50 T. Kammler, S. Wehner and J. Küppers, *Surf. Sci.*, 1995, **339**, 125–134.

51 D. Massiot, F. Fayon, M. Capron, I. King, S. Le Calvé, B. Alonso, J.-O. Durand, B. Bujoli, Z. Gan and G. Hoatson, *Magn. Reson. Chem.*, 2002, **40**, 70–76.

52 C. Copéret, A. Comas-Vives, M. P. Conley, D. P. Estes, A. Fedorov, V. Mougel, H. Nagae, F. Núñez-Zarur and P. A. Zhizhko, *Chem. Rev.*, 2016, **116**, 323–421.

53 L. Baggetto, V. Sarou-Kanian, P. Florian, A. N. Gleizes, D. Massiot and C. Vahlas, *Phys. Chem. Chem. Phys.*, 2017, **19**, 8101–8110.

54 S. K. Lee and C. W. Ahn, *Sci. Rep.*, 2014, **4**, 4200.

55 V. Sarou-Kanian, A. N. Gleizes, P. Florian, D. Samélor, D. Massiot and C. Vahlas, *J. Phys. Chem. C*, 2013, **117**, 21965–21971.

56 P. M. Abdala, O. V. Safonova, G. Wiker, W. van Beek, H. Emerich, J. A. van Bokhoven, J. Sá, J. Szlachetko and M. Nachtegaal, *Chimia*, 2012, **66**, 699–705.

57 L. Zhou, L. Li, N. Wei, J. Li and J.-M. Basset, *ChemCatChem*, 2015, **7**, 2508–2516.

58 E. J. M. Hensen, D. G. Poduval, P. C. M. M. Magusin, A. E. Coumans and J. A. R. V. Veen, *J. Catal.*, 2010, **269**, 201–218.

7576 | *Catal. Sci. Technol.*, 2021, **11**, 7563–7577

This journal is © The Royal Society of Chemistry 2021

59 A. Omegna, J. A. van Bokhoven and R. Prins, *J. Phys. Chem. B*, 2003, **107**, 8854–8860.

60 M. F. Williams, B. Fonfé, C. Sievers, A. Abraham, J. A. van Bokhoven, A. Jentys, J. A. R. van Veen and J. A. Lercher, *J. Catal.*, 2007, **251**, 485–496.

61 K. Monu, L. César, C. Zixuan, G. David, W. Elena, M. Christoph, F. Franck, M. Dominique, F. Alexey, C. Christophe, L. Anne and F. Pierre, *Atomic-Scale Structure and its Impact on Chemical Properties of Aluminum Oxide Layers Prepared by Atomic Layer Deposition on Silica*, 2021.

62 J. A. Bokhoven, D. C. Koningsberger, P. Kunkeler, H. van Bekkum and A. P. M. Kentgens, *J. Am. Chem. Soc.*, 2000, **122**, 12842–12847.

63 E. Bourgeat-Lami, P. Massiani, F. Di Renzo, P. Espiau, F. Fajula and T. Des Courières, *Appl. Catal.*, 1991, **72**, 139–152.

64 B. H. Babu, M. Niu, X. Yang, Y. Wang, L. Feng, W. Qin and X.-T. Hao, *Opt. Mater.*, 2017, **72**, 501–507.

65 A. K. Yadav and P. Singh, *RSC Adv.*, 2015, **5**, 67583–67609.

66 K. Chah, B. Boizot, B. Reynard, D. Ghaleb and G. Petite, *Nucl. Instrum. Methods Phys. Res., Sect. B*, 2002, **191**, 337–341.

67 J. W. Chan, T. Huser, S. Risbud and D. M. Krol, *Opt. Lett.*, 2001, **26**, 1726–1728.

68 M. Sakakura, M. Terazima, Y. Shimotsuma, K. Miura and K. Hirao, *J. Appl. Phys.*, 2011, **109**, 023503.

69 M. Okuno, N. Zotov, M. Schmücker and H. Schneider, *J. Non-Cryst. Solids*, 2005, **351**, 1032–1038.

70 P. Du, P. Zheng, S. Song, X. Wang, M. Zhang, K. Chi, C. Xu, A. Duan and Z. Zhao, *RSC Adv.*, 2016, **6**, 1018–1026.

71 R. Huirache-Acuña, T. A. Zepeda, E. M. Rivera-Muñoz, R. Nava, C. V. Loricera and B. Pawelec, *Fuel*, 2015, **149**, 149–161.

72 E. J. M. Hensen, D. G. Poduval, V. Degirmenci, D. A. J. M. Ligthart, W. Chen, F. Maugé, M. S. Rigutto and J. A. R. V. Veen, *J. Phys. Chem. C*, 2012, **116**, 21416–21429.

73 C. Jiménez-González, Z. Boukha, B. de Rivas, J. R. González-Velasco, J. I. Gutiérrez-Ortiz and R. López-Fonseca, *Energy Fuels*, 2014, **28**, 7109–7121.

74 Q. Liu, J. Gao, M. Zhang, H. Li, F. Gu, G. Xu, Z. Zhong and F. Su, *RSC Adv.*, 2014, **4**, 16094–16103.

75 J. Gao, C. Jia, M. Zhang, F. Gu, G. Xu and F. Su, *Catal. Sci. Technol.*, 2013, **3**, 2009–2015.

76 C. Jia, J. Gao, J. Li, F. Gu, G. Xu, Z. Zhong and F. Su, *Catal. Sci. Technol.*, 2013, **3**, 490–499.

77 N. Miletić, U. Izquierdo, I. Obregón, K. Bizkarra, I. Agirrezabal-Telleria, L. V. Bario and P. L. Arias, *Catal. Sci. Technol.*, 2015, **5**, 1704–1715.

78 W. Tsai, J. A. Schwarz and C. T. Driscoll, *J. Catal.*, 1982, **78**, 88–95.

79 J. Zhang, H. Xu, X. Jin, Q. Ge and W. Li, *Appl. Catal., A*, 2005, **290**, 87–96.

80 C. Guimon, N. El Horr, E. Romero and A. Monzon, in *Stud. Surf. Sci. Catal.*, ed. A. Corma, F. V. Melo, S. Mendioroz and J. L. G. Fierro, Elsevier, 2000, vol. 130, pp. 3345–3350.

81 S. He, H. Wu, W. Yu, L. Mo, H. Lou and X. Zheng, *Int. J. Hydrogen Energy*, 2009, **34**, 839–843.

82 J. Guo, H. Lou and X. Zheng, *Carbon*, 2007, **45**, 1314–1321.

83 P. Wang, E. Tanabe, K. Ito, J. Jia, H. Morioka, T. Shishido and K. Takehira, *Appl. Catal., A*, 2002, **231**, 35–44.

84 P. Mallet-Ladeira, P. Puech, C. Toulouse, M. Cazayous, N. Ratel-Ramond, P. Weisbecker, G. L. Vignoles and M. Monthioux, *Carbon*, 2014, **80**, 629–639.

85 T. Sodesawa, A. Dobashi and F. Nozaki, *React. Kinet. Catal. Lett.*, 1979, **12**, 107–111.

This journal is © The Royal Society of Chemistry 2021

Catal. Sci. Technol., 2021, **11**, 7563–7577 | **7577**